

Evaluation of the Turbulence Model Effects on the Flow Field and Sound Pressure Levels Generated by Small Caliber Weapons System

Seyda Ozbektas[#], Bilal Sungur^{§,*} and Onur Gurdamar[§]

[#]Department of Mechanical Engineering, Ondokuz Mayıs University, Samsun, Turkey

[§]Department of Mechanical Engineering, Samsun University, Samsun, Turkey

*E-mail: bilal.sungur@samsun.edu.tr

ABSTRACT

Estimation of the flow field around the projectile is crucial to predict the high-intensity noise. In this study, the effects of turbulence models on the flow field and far-field noise generated during the blast flow of a small caliber gun were investigated numerically. In this context, the numerical simulations of the influence of different turbulence models were performed for two different ammunition models, where in one case the projectile at the muzzle of the barrel had a subsonic velocity, and in the other case the projectile's initial velocity was supersonic. The small caliber 9x19 mm gun was selected in accordance with this purpose. To predict the far-field noise in numerical modeling, Ffowcs Williams and Hawkins acoustic analogies (FW-H) equations were solved in two-dimensional, axisymmetric, transient conditions. To see the effects of turbulence models on results, k- ϵ models (Standard, RNG, Realizable), Standard k- ω , Spalart-Allmaras and LES turbulence models were used. Also, to model the moving projectile where the ballistic domain changed with time, a dynamic mesh model was used. The results of the numerical simulation obtained on the RNG k- ϵ turbulence model, in comparison with the experimental results, give better agreement for projectiles with a subsonic initial velocity. For projectiles that have supersonic velocity, the best results are given by numerical simulations where Spalart-Allmaras turbulence model was used. Therefore, by assuming two-dimensional and single-phase gas, where the chamber pressure and temperature are known and angular momentum of projectile is neglected, these models can be used as a quick tool to estimate the far-field noise from a small-caliber gun during the design stage.

Keywords: Muzzle flow field; Sound pressure; Numerical simulation; Firearm

1. INTRODUCTION

During the firing of small caliber guns, the gunpowder in the projectile casing combusts, generating a high-intensity noise as a muzzle blast wave. When shooting a gun, there are three main sources of noise: the muzzle blast, the sonic boom, and the mechanical noises caused by the interior moving parts. Muzzle blasts arise from many factors, such as unstable shock waves in muzzle flow or turbulent fluctuation in the mixing zone. Many of these noises decrease and disappear at the initial stage of forming the muzzle flow field. The main impulse noise occurs by the propelled gas turbulent jet in the muzzle system¹⁻².

The rapid release of chemical energy from the propellant in a firearm produces muzzle blast and flash phenomena within a matter of milliseconds. A schematic view of the dynamic wave process occurring at the muzzle during a gunshot was shown Fig. 1. The sudden discharge is usually characterized by a fuel-rich composition, mixing with turbulent air drawn from the surroundings. As a bullet passes through the barrel exit, a main shock wave is produced that clings to the bullet during its movement. The expelled propellant gas produces both a normal shock and an oblique shock wave. Additionally, the jet

boundary occurs enclosing these two wave types. Inside the region (I) defined by the normal and oblique shock waves, the flow velocity is supersonic. Besides, the flow is supersonic in the region (II) between the jet and oblique boundaries. On the other hand, in region (III) behind the main shock, the velocity

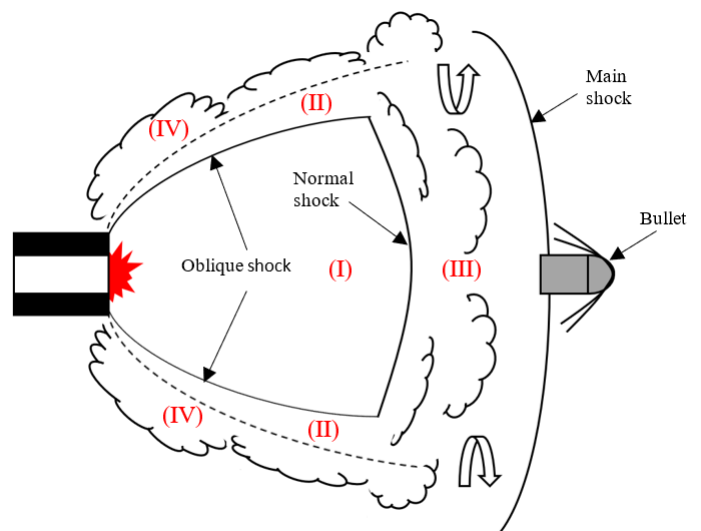


Figure 1. Schematic view of the dynamic wave process occurring at the muzzle during a gunshot.

is subsonic and numerous vortices occur in this region. In region (IV), which lies outside the jet boundary, turbulence rings occur due to the interaction of the jet flow with the surrounding air. In both regions (III) and (IV), the main shock and air disturbance serve as acoustic sources, contributing to the noises heard by receivers³.

In Computational Fluid Dynamics (CFD), the turbulence model has a critical impact on the numerical simulation of projectile motion. There are three main categories in the solution of turbulent flow, which are Direct Numerical Simulation (DNS), Large Eddy Simulation (LES), and Reynolds-Averaged Navier–Stokes Simulation (RANS)⁴. The most accurate method is the DNS method⁵⁻⁶, but it requires a high-demand computer. In this method, turbulent flow is obtained directly by solving the Navier-Stokes equations. In the LES method^{2,7}, low-pass filtering is applied in the Navier-Stokes equations to lower resolution on time scales, directly resolving large-scale eddies in turbulent flow. The LES method has high calculation accuracy and is used in engineering calculations. The RANS method⁸⁻⁹ presents good results in engineering applications and saves time. In this method, the flow degraded into time average and instantaneous pulsating flows, which were solved separately.

A lot of research has been done in the literature to model the projectile motion and to see the effect of this motion and noise levels. Jiang¹⁰, *et al.* employed a flat-nose in the projectile to research the jet-flow and shock-wave interactions of the flow field created by a supersonic projectile. Luo¹¹, *et al.* realized numerical calculations to study the dynamical processes induced by a projectile launched from a gun into the surrounding air. Trabinski¹², *et al.* studied the dynamic characteristics of the flow field around a projectile for situations with and without a muzzle device. The mechanism behind the creation of the bow shock wave in front of the projectile was examined by Kikuchi, *et al.* both experimentally and numerically¹³. Kang¹⁴, *et al.* carried out a numerical study on the reduction of noise levels emitted from the shock tube in a high pressure explosion. Xavier¹⁵ analysed the pressure and sound distribution of a firearm for a bullet by setting the pressure and temperature values to 3450 atm and 2500 K, respectively, in a 200 mm long barrel. He also examined the effect of bullet mass, pressure and temperature on the flow field. Huerta-Torres, *et al.*¹⁶ numerically and experimentally the effect of a suppressor on noise in a 5.56 mm caliber rifle. Hudson¹⁷, *et al.* examined the accuracy of the computational models used in the design of suppressors for small-caliber weapons. In this context, they developed a model suppressor and conducted simulations and experiments. They stated that current simulations can accurately predict the acoustic signal levels.

Due to the complex characteristics of the flow field, there are few studies in the literature on the computation and estimation of the muzzle noise field, particularly the far-field noise. It is difficult to observe changes in the flow field experimentally, and experiments do not show how the noise field at the barrel exit is propagated as a result of gunfire. Additionally, shooting tests requires a lot of money and time. CFD programs can simulate the flow in the region close to

the barrel exit and predict the noise with ease, but it fails to handle for muzzle noise in far fields. Many researchers looked into CFD-CAA hybrid methods as an alternative method in this context^{2,18-21}. Zhao², *et al.* focused on impulse noise generated by complex jet streams from small-caliber rifles with muzzle suppressors. They claimed that the muzzle suppressor affected the flow field and the direction of the sound based on the results of their simulations. Lee¹⁹, *et al.* estimated the noise field with and without silencers using a CFD-CAA coupled method at two dimensional conditions. Wang²⁰, *et al.* employed the FW-H model to determine the small caliber rifle's noise discharging directivity. Bin¹⁸, *et al.* conducted a numerical study on the impulse noise generated by complex flows discharged from a barrel. The complex flow properties and noise generation mechanisms around the muzzle were numerically discussed. In their calculations, they realized a two-dimensional axisymmetric solution. Based on the results of their study, they stated that computational aeroacoustic (CAA) provides a method to examine the blast wave dynamics of muzzle flow. Zhao²¹, *et al.* used CFD-CAA coupled method to evaluate the impulse noise and targeting efficiency of muzzle brake. Gurdamar²², *et al.* studied both experimentally and numerically the effect of the number of circular ring baffles in the suppressor and the distance between them on the flow field and the sound in the far field in a 9 mm semi-automatic pistol.

The majority of papers discussed in the literature relate to the development of muzzle brakes, suppressors, and silencers to lessen the intensity of sound generated during explosion and their impact on flow around barrel. Also in most studies, effect of the projectile on the flow field and the post-explosion noise analyzed separately. The studies investigating the correlation of turbulence models with these parameters are limited. Here, we address to fill this gap in the literature. In this study, the effects of turbulence models on the flow field and Sound Pressure Level (SPL) of the 9x19 mm semi-automatic pistol were investigated numerically. In this context, k- ϵ models (Standard, Realizable, RNG), Standard k- ω , Spalart-Allmaras and LES turbulence models were used as turbulence models and the sound pressure level was obtained by solving Ffowcs Williams and Hawkings (FW-H) equations. The results were compared with experimental measurements for subsonic and supersonic projectiles. The findings of this research are valuable for predicting barrel noise and optimizing the most appropriate turbulence model for small-caliber weapon systems.

2. METHODOLOGY

2.1 Experimental Setup

Shooting tests with gun took place outdoor. The main components of the experimental setup were a table, gun stabilizer, Larson Davis LXT sound level meter, Labrador Ballistic Velocity Doppler Radar Chronograph, and a 9x19 mm gun (Canik TP9 Elite Combat model). The schematic illustration of the experimental installation was given in Fig. 2. The gun was mounted to a stabilizer on a table one meter above the ground in order to prevent sound reflection. For gunshot tests, subsonic and supersonic projectiles were employed. In all experiments, the microphone was mounted vertically with the tripod's height aligned with the axis of the gun barrel. In all

gunshot tests, the y distance was kept constant at 0.2 m and the x distances were set as 1 m, 1.5 m, 2 m, 2.5 m, 5 m, 10 m, 20 m and 30 m, respectively. For each location where the peak sound pressure level (SPL_{peak}) was measured, six shots were fired from the gun at intervals of ten seconds. The CAL200 sound level calibrator was used to test the microphone calibration before the tests began. The details of the experiments can be found in Reference 23.

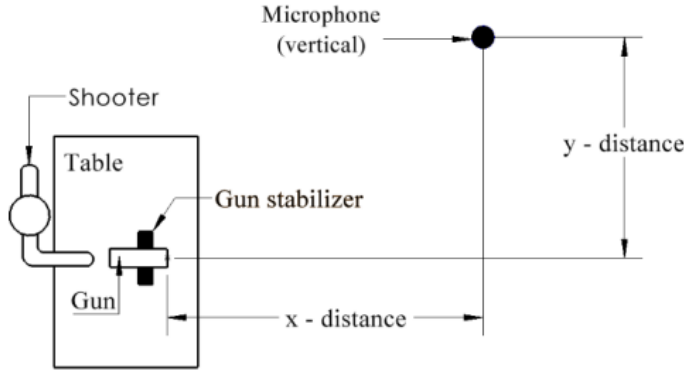


Figure 2. The schematic illustration of the experimental installation.

2.2 Numerical Method

2.2.1 Acoustic Analogy

Strong vortices and shock waves that emanate from the muzzle of firearms typically cause noise. High pressure and temperature create an unstable flow field at the barrel exit when a gun is fired. This flow field’s energy is also much higher than the energy of sound. It is challenging to numerically calculate the sound waves in these kinds of situations. Computational Fluid Dynamics (CFD) and Computational Aeroacoustics (CAA) can be analyzed together thanks to a hybrid approach offered by Ansys Fluent. The Lighthill acoustic analogy equation obtained by rearranging the mass and momentum equations is used to develop aerodynamic acoustics²⁴. The Navier-Stokes equations are used to derive the sound source term in this equation. Lighthill starts from the continuity and momentum Eqn. which, by using the summation convention, can be written as

$$\frac{\partial \rho}{\partial t} + \frac{\partial \rho u_j}{\partial x_j} = 0 \tag{1}$$

$$\rho \frac{\partial u_i}{\partial t} + u_j \frac{\partial \rho u_i}{\partial x_j} = -\frac{\partial p}{\partial x_i} - \frac{\partial \tau_{ij}}{\partial x_j} \tag{2}$$

In Eqn. (1) and (2), ρ denotes the density of the fluid, v_i the i -th component of the flow velocity vector \mathbf{v} , p the overall pressure and τ_{ij} the (i, j) th component of the viscous stress tensor. For a Stokesian gas it can be expressed in terms of the velocity gradients by

$$\tau_{ij} = -\mu \left(\frac{\partial u_i}{\partial x_j} + \frac{\partial u_j}{\partial x_i} - \frac{2}{3} \mu \delta_{ij} \frac{\partial u_k}{\partial x_k} \right) \tag{3}$$

where, μ is the viscosity of the fluid and δ_{ij} is the Kronecker delta.

Multiplying the continuity in Eqn. (1) by u_i , adding the result to the momentum equation, and combining terms yields

$$\frac{\partial \rho u_i}{\partial t} = -\frac{\partial}{\partial x_j} (\rho u_i u_j + \delta_{ij} p + \tau_{ij}) \tag{4}$$

which after adding and subtracting the term $c \frac{\partial \rho}{\partial x_i}$ (c_0 denotes the speed of sound), becomes

$$\frac{\partial \rho u_i}{\partial t} + c_0^2 \frac{\partial \rho}{\partial x_i} = -\frac{\partial T_{ij}}{\partial x_j} \tag{5}$$

In Eqn. (5), T_{ij} denotes Lighthill’s stress tensor given as

$$T_{ij} = \rho u_i u_j + \delta_{ij} [(p - p_0) - c^2 (\rho - \rho_0)] + \tau_{ij} \tag{6}$$

With ρ_0 and p_0 the atmospheric values of density and pressure respectively. It is possible to differentiate Eqn. (1) with respect to t , take the divergence of Eqn. (5), and subtract the results to obtain Lighthill’s inhomogeneous wave equation solving for the acoustic density ρ'

$$\frac{\partial^2 \rho'}{\partial t^2} - c_0^2 \frac{\partial^2 \rho'}{\partial x_i^2} = \frac{\partial^2 T_{ij}}{\partial x_i \partial x_j} \tag{7}$$

An important aspect in Lighthill’s acoustic analogy, in order to be able to compute the noise radiation, is the assumption that Lighthill’s stress tensor is a known source term or at least can be evaluated to a certain degree of approximation. Additionally, this source term is assumed to vanish outside the turbulent region²⁵.

The Ffowcs Williams and Hawkings Acoustics Model was employed in this study to calculate the far-field noise. This model simultaneously calculates sound pressure signals at predetermined receivers. The Lighthill acoustic analogy serves as the basis for the FW-H Eqn. The impermeable surface in the flow is taken into account by this inhomogeneous wave Eqn. Monopole, dipole, and quadrupole are the three inhomogeneous terms in this Eqn. Unsteady mass injection produces a source called the monopole acoustic source. Two monopole sources coming from unsteady external forces compose a dipole acoustic source. Two dipole sources coming from unsteady shear stresses compose a quadrupole acoustic source. The sound produced by a body moving through a flow is represented by the monopole and dipole terms combined²⁶. In Eqn. (8), the FW-H Eqn. is presented.

$$\begin{aligned} \frac{1}{c_0^2} \frac{\partial^2 p'}{\partial t^2} - \nabla^2 p' = & \frac{\partial^2}{\partial x_i \partial x_j} \{T_{ij} H(f)\} \text{ (monopole)} \\ & - \frac{\partial}{\partial x_i} \{ [P_{ij} n_j + \rho u_i (u_n - v_n)] \delta(f) \} \text{ (dipole)} \\ & + \frac{\partial}{\partial t} \{ [\rho_0 v_n + \rho (u_n - v_n)] \delta(f) \} \text{ (quadrupole)} \end{aligned} \tag{8}$$

$$P_{ij} = p \delta_{ij} - \mu \left[\frac{\partial u_i}{\partial x_j} + \frac{\partial u_j}{\partial x_i} - \frac{2}{3} \frac{\partial u_k}{\partial x_k} \delta_{ij} \right] \tag{9}$$

The acoustic source surface is designated as $f=0$ in Eqn. (8). Fluid velocity component in the x_i direction is represented by u_i , and those in the direction normal to the acoustic surface by u_n . The surface velocity component normal to the acoustic surface is expressed by v_n . Heaviside and Dirac delta functions are represented by $H(f)$ and $\delta(f)$, respectively. The difference between the atmospheric pressure in the environment and the immediate pressure at the location where a sound wave exists is known as sound pressure. It is shown with the formula

$p' = p - p_0$. The compressive stress tensor is expressed by P_{ij} in Eqn. (9).

SPL is a logarithmic (decibel) measurement of sound pressure in relation to the reference hearing threshold value. It is determined using the formula in Eqn. (10). The lowest level of sound that a human can hear is expressed as p_{ref} , which is usually 2×10^{-5} Pa.

$$SPL = 20 \log \frac{p'}{p_{ref}} \quad (10)$$

2.2.2 Boundary Conditions and Geometry

Within the scope of this study, the flow in near-field and sound emitted in far-field during the firing of a 9x19 mm gun were tried to be estimated numerically by using different turbulence models. In this context, the calculations were performed using the Fluent package program, which allows solving the flow field and aeroacoustics together. The pressure of the external environment was 1atm and the temperature was 300 K. Pressure and temperature values for subsonic and supersonic projectiles were taken according to manufacturer data and the literature^{2,21,27}. In this context, the volume behind the projectile was considered as a high-pressure chamber and pressure and temperature values of the chamber were patched as 1600 atm and 1800 K, respectively. As the projectile continued to move along the barrel, these pressure and temperature values decreased. For the supersonic projectile, the pressure value was increased to 2800 atm at the same temperature with subsonic projectile. At the boundaries of the projectile and barrel, wall boundary condition was adopted. The no-slip condition was used to ensure that the velocity at these wall boundaries was zero. On the left side of the external environment, the pressure inlet boundary condition was applied, with the total pressure and temperature both set to 1 atm and 300 K, respectively. The pressure outlet boundary condition was adopted in the right and upper sides of the computational domain. Fig. 3(a)

illustrated the boundary conditions that were used in the analysis. Solutions were obtained under conditions that were two-dimensionally axisymmetric, density-based, and time-dependent. In all analyses, air density was calculated using the Soave Redlich Kwong real gas model. To model turbulent flow, k-ε (Standard, Realizable, RNG), Standard k-ω, Spalart-Allmaras and LES turbulence models were used. Advection Upstream Splitting Method (AUSM) was utilized as the flow type, and Implicit Formulation was employed as the solution approach. For all equations, the convergence criterion was set to 10^{-3} .

In order to determine the noise emitted from the projectile exiting the barrel, three circular sound sources were placed to the external environment. In the estimation of far-field noise emitted from the near field for 2-D flow field, the third dimension can be included in the calculations by defining a Sound Correlation Length (SCL)⁴⁻⁷. Analyses of the flow and acoustics were started simultaneously. In acoustic model, receivers were placed where SPL measurements were carried out in the experiments.

As mentioned above, the geometry consisted of the static domain forming the external environment and the dynamic domain in which the projectile motion occurred. The solution was performed in 2D and axisymmetric conditions. The total length and width of the solution domain where the calculations were carried out were 725 mm and 127 mm, respectively. The projectile had 9 mm diameter and 7 mm length. The gun barrel had 100 mm length and 2 mm wall thickness. The projectile was placed inside the gun barrel. The distance between the base of the projectile and the breech of the gun barrel was 12 mm. In addition, the distance between the front of the projectile and the barrel exit was 81 mm. Three sound sources were placed in the external environment to be used in the acoustic analysis. They were modeled as circular geometry with a 1 mm diameter so that these sound sources had negligible effects on the flow

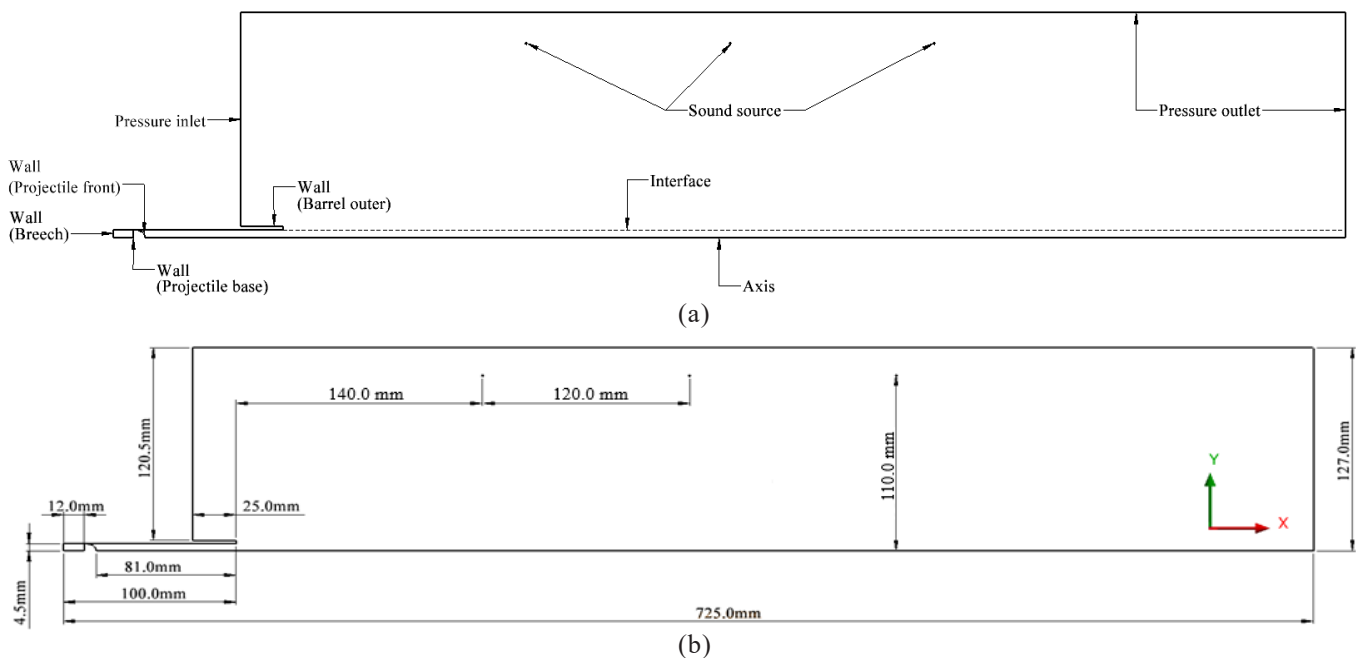


Figure 3. (a) Boundary conditions, and (b) dimensions of the geometry.

field. The dimensions of the geometry used in numerical modeling were given in Fig. 3(b).

Some studies in the literature modelled projectile movement in 2D and axisymmetric conditions using a Six-DOF model^{3,11,27}. In this study, the internal ballistic problem of the projectile was defined within the framework of following assumptions:

- The barrel and the core were axisymmetric, cylindrical around the x axis
- Gravity was neglected
- The chamber gas pressure is uniform
- Heat transfer from the barrel was neglected
- The projectile was only allowed to move in the longitudinal direction of the barrel
- The angular momentum equation was neglected
- The mass of bullet (core) was 3.2897 g
- Propellant gas and the external environment fluid were modelled as single-phase and homogeneously miscible.

2.2.3 Mesh Structure

Boundary conditions in the geometry varied depending on time while modeling a projectile motion along the barrel. Therefore, the dynamic mesh structure with a moving boundary was used to model the unsteady flow. The projectile's movement field was defined as rigid, and its immediate surrounding was defined as stationary. In the rigid region, the mesh element type was selected as rectangular, and the layering method, which works more stable in this element type, was employed as the dynamic mesh method. According to the layer height next to the moving surface, this method attaches or detaches cell layers next to moving boundary²⁴. To simulate the freedom of movement of the projectile along the barrel, Six Degrees of Freedom (Six-DOF) was activated. The projectile weight was entered as 3.2897 gr. The front and base of the projectile were defined as rigid.

The determined pressure in the barrel was employed to propel the projectile in this study. Fluent provides the capability to address the equations governing the movement of a rigid body with six degrees of freedom. In this context, the body is characterized by various surfaces, specifically the wall surfaces of the projectile. The equation of motion for a rigid body can be expressed in accordance with Eqn. (11) and (12), which the rate of change of linear and angular momentum P and L are equal to the applied force and torque F and M , respectively²⁸.

$$\frac{dP}{dt} = F \quad (11)$$

$$\frac{dL}{dt} = M \quad (12)$$

To address the angular momentum equations, it is essential to compute the moments of inertia for the body. The rotational velocity of the projectile remains almost constant within the rigid domain examined in this study. Two approaches can be employed to implement the rotation of the projectile: utilizing the rigid body or specifying a velocity on the projectile wall. Implementing rotation through the rigid body method will be challenging, as it requires the projectile to rotate within the mesh and this method has not been incorporated into the model. Alternatively, employing the projectile wall and defining a rotational velocity in the boundary conditions offers a more straightforward implementation of rotation in the model. This approach ensures a consistent rotational velocity throughout the entire simulation. Though it is acknowledged that the projectile maintains approximately 90 per cent of its rotational velocity until reaching the target. Consequently, the change in angular momentum near the muzzle, which is in focus in this work, will be negligible.

In this study, the projectile was only allowed to move in the longitudinal direction of the barrel and the angular momentum equation was neglected. Therefore, 1 DOF model

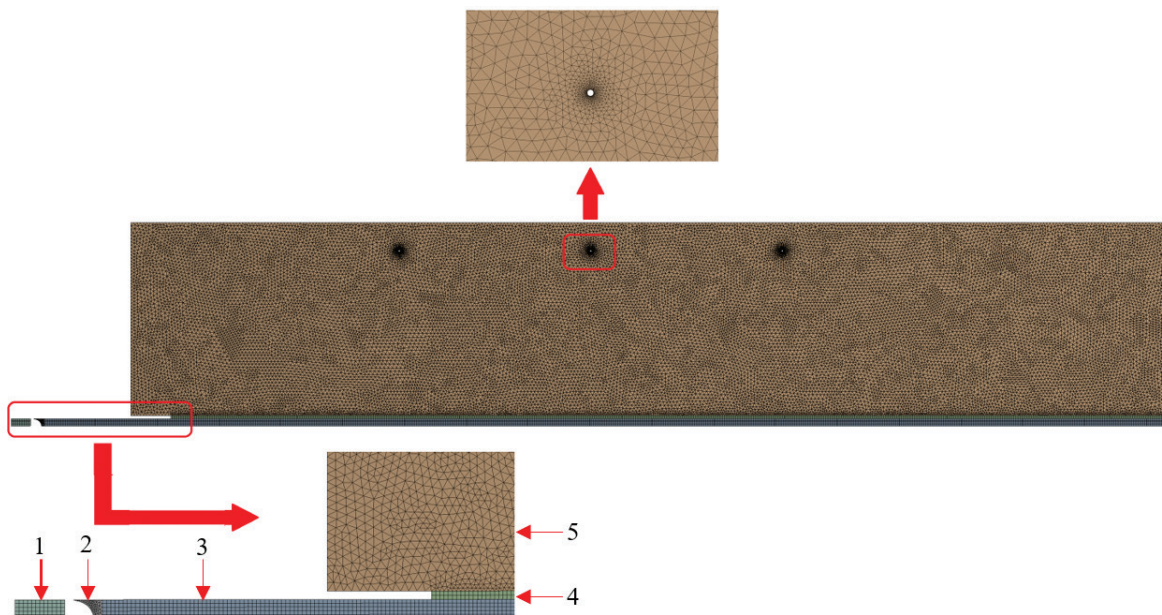
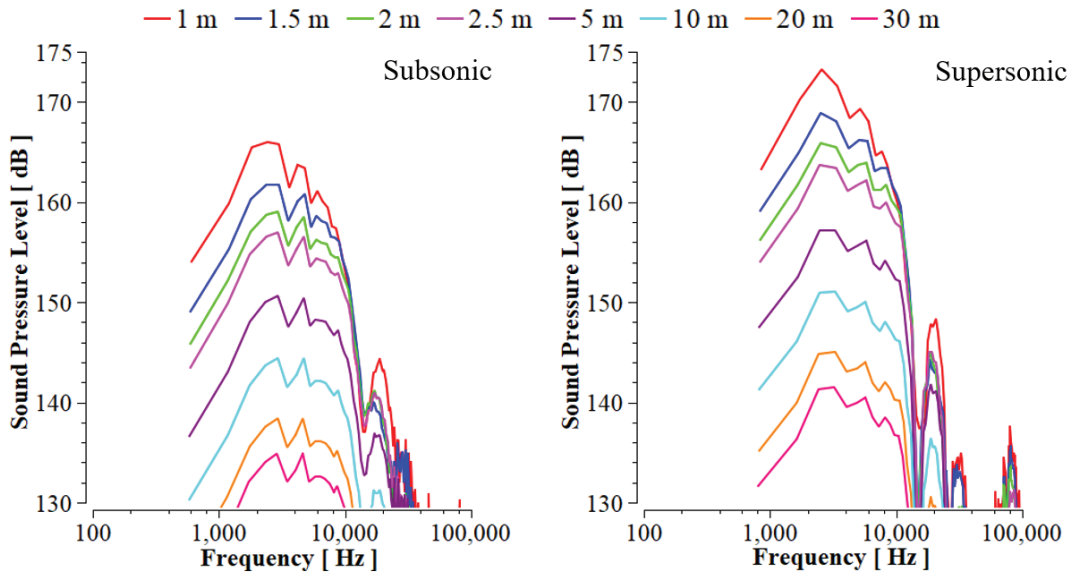
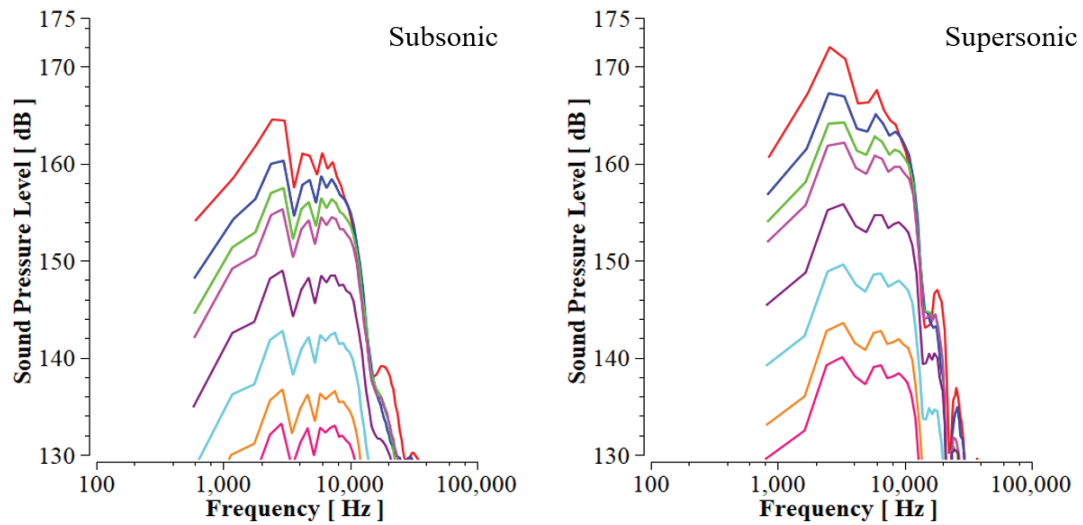


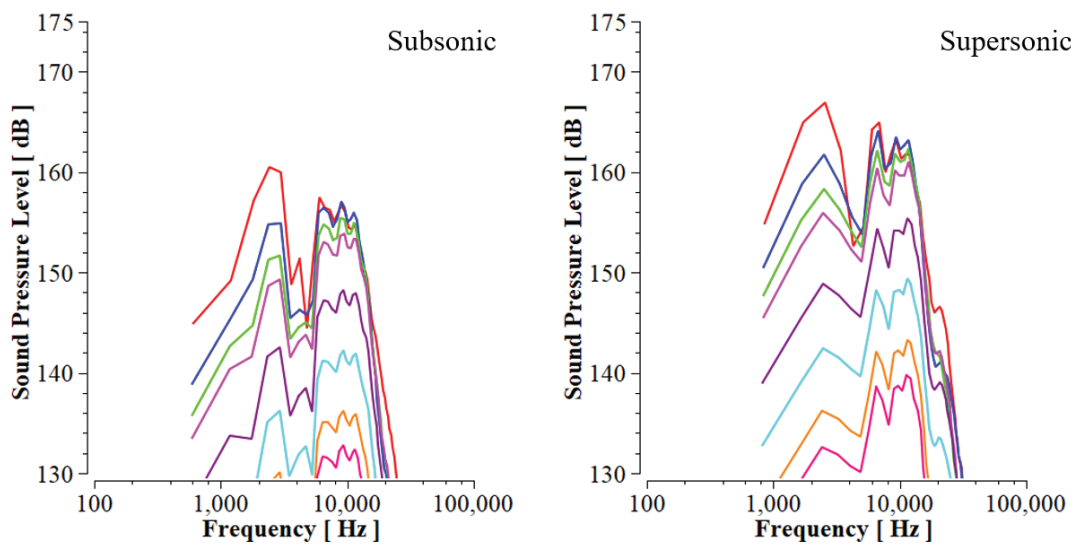
Figure 4. The view of the mesh structure.



Standart k-ε



RNG k-ε



Realizable k-ε

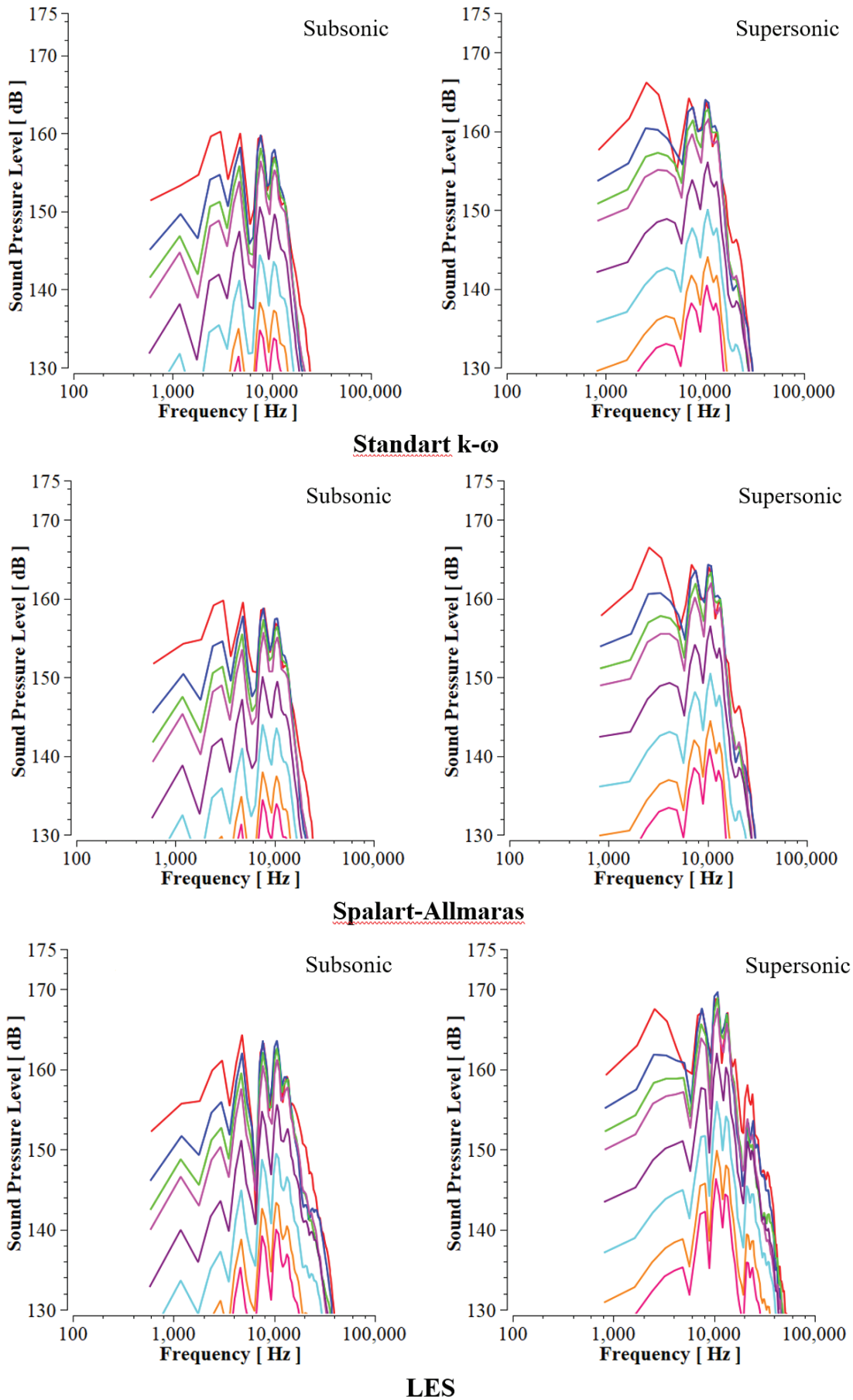


Figure 5. Variations of SPL with frequency at different distances.

was used in this study. The Eqn. of linear momentum could be simplified to the following one-dimensional problem.

$$m\ddot{x} = \dot{\mathbf{u}} = F_{Aero} + F_{Ext} \quad (13)$$

where, x is position in the direction of the translation, m is the mass of the projectile, F_{Aero} is the resulting aerodynamic force (i.e. drag, lift) and F_{Ext} is an applied external force, for instance friction between the barrel and the projectile. Eqn. (13) is solved iteratively in Fluent by use of the Newmark integration scheme²⁸.

In this study, dynamic mesh was used and in this context the mesh quality varied with time. The CFD domain was divided into several smaller domains to apply different mesh methods and sizes. The view of the mesh structure used in numerical modeling was given in Fig. 4. Domain 1 was the high-pressure chamber which gave the projectile the initial motion, and domain 2 was the front side of the projectile. Domain 3 illustrated the field where the projectile moves until the muzzle exit. Domains 4 and 5 were the external environment where the flow field was calculated. The triangle mesh structure was used in domains 2 and 5. Rectangular mesh structure was used in domains 1 and 3 because it was suitable for the layering method. In addition, domain 4 also had a rectangular mesh structure. When the mesh structures were examined in terms of size, domains 1, 3 and 4 had a mesh size of 1 mm.

The mesh size of 0.5 mm was used in domain 2 to give the curvature in front of the projectile. On the other hand, the external environment had a relatively coarser mesh structure than other domains. In this context, a mesh size of 2 mm was used in domain 5. Around the sound sources, the mesh edge size was 0.1 mm, and the growth rate was 1.2. The mesh structure created consisted of a total of 29172 nodes and 50871 elements. For a good mesh structure, the element quality should be close to 1, the skewness to 0, and the orthogonal quality to 1²⁴. In this mesh structure, average element quality, skewness and orthogonal quality were 0.96, 0.05 and 0.97, respectively.

3. RESULTS AND DISCUSSION

In this study, the velocity, temperature and pressure distributions in the external environment surrounding the barrel occurred by supersonic and subsonic projectiles fired from a 9x19 mm semi-automatic pistol were investigated and the sound emitted in the far-field was estimated. The program fluent package was employed, which can solve both the aeroacoustic and flow fields simultaneously. The FW-H acoustics model was selected to estimate the sound emitted in the far-field. The Fast Fourier transform (FFT) was used to post-process the acoustic pressure signals. Flow analyses were carried out using six different turbulence models to investigate the effects of turbulence models on sound estimation. In this context, k- ϵ models (Standard, Realizable, RNG), Standard k- ω , Spalart-Allmaras and LES turbulence models were used, and the sound data obtained from these models were compared with each other. In all calculations, the aeroacoustic model and flow analysis were started simultaneously. SPLs were investigated in the numerical model, as in the experimental study, in the direction of the barrel axis and at distances of 1.0 m, 1.5 m, 2.0, 2.5 m, 5.0 m, 10.0 m, 20.0 m and 30.0 m

from the barrel exit. The peak sound pressure levels (SPL_{peak}) obtained from the numerical model were compared with the experimental results. The temperature, velocity and pressure contours in the flow field of the turbulence model, which gave the closest result to the experimental measurements, were shown in this study.

According to the manufacturer data, the maximum velocity range of the subsonic projectile is 280-300 m/s, while it is between 360-380 m/s for the supersonic projectile. As said before, projectile velocities were also measured experimentally in this study and the velocity at the barrel exit was 317 m/s for the subsonic projectile and 382 m/s for the supersonic projectile. There is a slight difference between manufacturer's data and experimental measurements and this can be explained by the fact that projectile velocities in manufacturer data are generally measured based on a distance of 16 m. In numerical study, projectile velocities for different turbulence models had approximately the same values. In this context, the maximum velocity for the subsonic projectile was approximately 301 m/s, while the maximum velocity for the supersonic projectile was approximately 375 m/s. Because the projectile moved at these velocities and the flow field had a limited length, 0.005 ms time step was selected while calculating the development of the flow outside the barrel. In this time step, the sound pressure graphs obtained from the acoustic analysis were drawn in the range of 100-500000 frequency.

The variation graphs of SPLs with frequency for subsonic and supersonic projectiles at different distances were given in Fig. 5. According to the graphs obtained from the acoustic analysis, SPL dropped rapidly after peaking at low frequencies and oscillated roughly in the range of 60-120 dB in the frequency range of 100k-500k Hz. SPL decreased with increasing distance in all analyzes, and SPL_{peak} values obtained from the supersonic projectile were higher than that of the subsonic projectile at all distances as expected. When the trend lines of the graphs were examined, it was seen that the Standard k- ϵ and RNG k- ϵ turbulence models followed a similar trend in the frequency ranges where SPL_{peak} values occurred. On the other hand, Standard k- ω , Spalart-Allmaras and LES turbulence models followed similar trend lines in frequency ranges where SPL_{peak} values occurred. These three models had a more oscillations trend than other models. SPL_{peak} values were obtained at lower frequencies in Standard and RNG k- ϵ turbulence models compared to other turbulence models. In this context, while the SPL_{peak} was between 2000-4000 Hz in Standard and RNG k- ϵ turbulence models, it varied between 7000-12000 Hz in other turbulence models.

The comparison of SPL_{peak} values obtained from different turbulence models with experimental results for subsonic and supersonic projectile was shown in Fig. 6. SPL_{peak} values decreased with increasing distance for both projectile models. An exception to this situation was the LES turbulence model for the supersonic projectile. In this case, the SPL_{peak} obtained at 1.5 m was slightly lower than that at 1 m. It was assumed that this was due to differences in sound propagation at supersonic velocity. For the subsonic projectile, the RNG k- ϵ turbulence model gave the SPL_{peak} values closest to the experimental measurements. In this context, the SPL_{peak} values at 1 m, 10

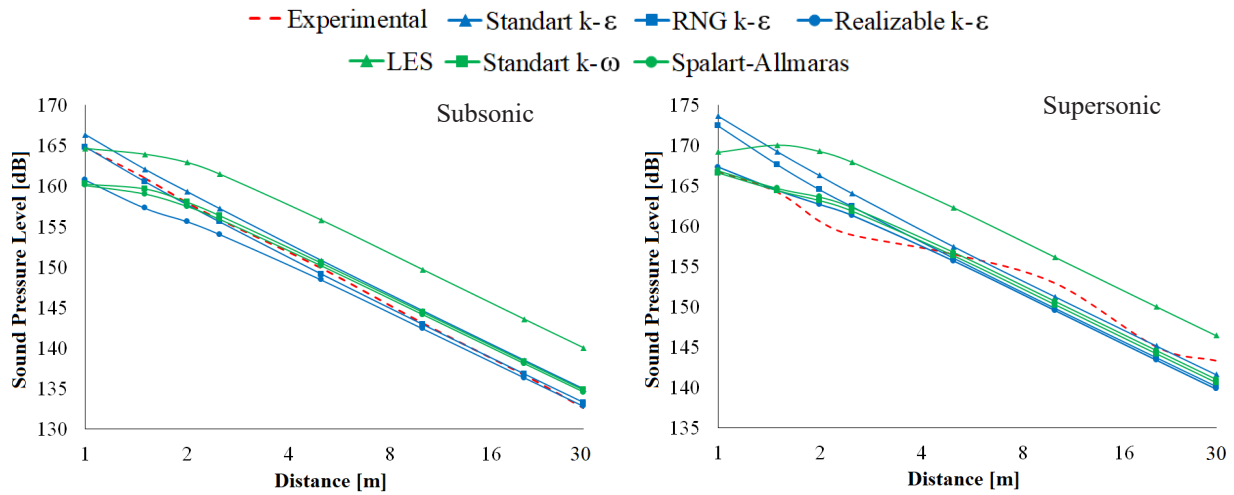


Figure 6. SPL_{peak} values obtained from different turbulence models.

Table 1. Error (%) in SPL_{peak} values for subsonic projectile

Turbulence model	Distance (m)								Average error
	1 m	1.5 m	2 m	2.5 m	5 m	10 m	20 m	30 m	
Standard k-ε	0.931	0.664	0.829	0.835	0.606	1.041	1.299	1.760	0.995
RNG k-ε	0.012	0.282	0.181	0.212	0.521	0.152	0.048	0.470	0.234
Realizable k-ε	2.467	2.313	1.509	1.203	0.994	0.510	0.281	0.139	1.177
LES	0.083	1.828	3.117	3.580	3.938	4.594	5.010	5.580	3.466
Standard k-ω	2.761	0.825	0.017	0.293	0.404	0.917	1.192	1.657	1.008
Spalart-Allmaras	2.861	1.225	0.318	0.005	0.169	0.704	0.988	1.451	0.965

Table 2. Error (%) in SPL_{peak} values for supersonic projectile

Turbulence model	Distance (m)								Average error
	1 m	1.5 m	2 m	2.5 m	5 m	10 m	20 m	30 m	
Standard k-ε	4.086	3.049	3.519	3.229	0.607	1.080	0.108	1.170	2.106
RNG k-ε	3.352	2.053	2.420	2.196	0.310	2.026	0.902	2.196	1.931
Realizable k-ε	0.293	0.124	1.284	1.504	0.536	2.209	1.116	2.424	1.186
LES	1.410	3.550	5.375	5.652	3.678	2.111	3.448	2.196	3.427
Standard k-ω	0.157	0.091	1.567	1.821	0.147	1.760	0.603	1.896	1.005
Spalart-Allmaras	0.014	0.277	1.862	2.122	0.145	1.472	0.308	1.599	0.974

m and 30 m distances were experimentally measured as 164.8 dB, 143.1 dB, 132.6 dB, and were numerically estimated with RNG k-ε turbulence model as 164.8 dB, 142.9 dB, 133.2 dB, respectively. On the other hand, the peak SPL_{peak} values closest to the experimental measurements for the supersonic projectile were estimated in the Spalart-Allmaras turbulence model. In this case, for the supersonic projectile, the SPL_{peak} values at 1 m, 10 m and 30 m distances were experimentally measured as 166.8 dB, 152.9 dB, 143.3 dB and numerically estimated as 166.8 dB, 150.6 dB, 141.0 dB, respectively. In addition to Spalart-Allmaras turbulence model, Standard k-ω and Realizable k-ε turbulence models also gave very close results to experimental measurements for the supersonic projectile. The differences between peak sound pressure levels obtained from experimental measurements and numerical solutions were given in Tables 1 and 2. As shown from these tables, especially at distances above 1 m, the worst SPL_{peak} values

were obtained in the LES turbulence model both with subsonic and supersonic projectiles.

When a gun fired, the high-pressure gas behind the projectile applies a thrust to the breech, and with this effect, the projectile moves towards the target. With this movement, the first precursor shock wave occurs at the barrel exit. This situation is followed by a series of compression waves.

The numerically obtained pressure, velocity and temperature contours for the subsonic projectile were shown in Fig. 7. In this figure, only the results of RNG k-ε turbulence model were given in which the SPL_{peak} values were best estimated.

In Fig. 7.a, the variation of the pressure distributions with time around the projectile were shown. The pressure values inside the barrel gradually continued to decrease from 1600 atm. However, for better illustration, the contour scale was limited with a special boundary condition of 2 atm. The gas

inside the barrel, which was at high pressure and temperature, expanded radially after ejecting from the barrel exit, as seen in this figure, and created a typical jet flow structure with bow, barrel, precursor, and seconder shock waves. When the projectile first came out of the barrel, high pressure occurred in front and side of the projectile, and negative pressure behind the projectile. The environment was affected by the gas that

was powerfully expelled from the barrel exit. The noise was produced as a result of this situation. The shock waves gradually diminished in strength as the projectile moved away from the barrel exit and spread over a larger field.

In Fig. 7(b), the variation of the velocity distributions with time around the projectile were shown. High velocities developed behind the projectile as a result of the pressure

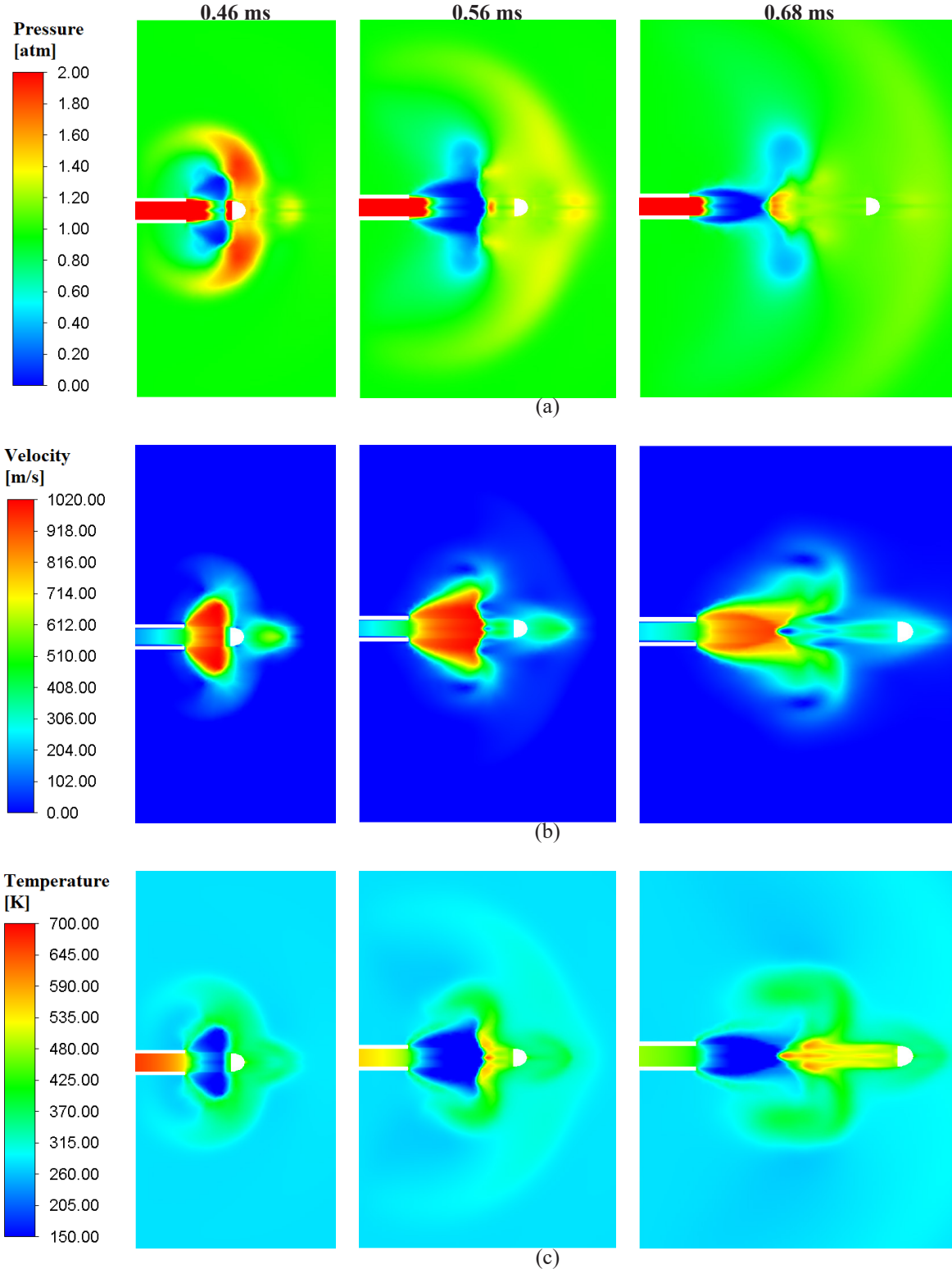


Figure 7. Contour views of the RNG k-ε turbulence model for subsonic projectile. (a) Pressure, (b) velocity and (c) temperature contours.

difference that resulted from the high-pressure air's interaction with the environment after the projectile left the barrel. During the time period examined in the figure, the velocities behind the projectile gradually decreased after reaching its peak at 0.46 ms. The range of the highest velocity values behind the projectile was 990-1020 m/s at 0.46 ms, 980-1015 m/s at 0.56 ms, and 900-940 m/s at 0.68 ms. In addition, friction with the surrounding air along the axial direction occurred as the jet flow expanded further. The local flow shifted in the opposite direction as a result of this situation.

In Fig. 7(c), the variation of the temperature distributions with time around the projectile was shown. When the projectile exited the barrel, the temperatures just behind the projectile dropped considerably due to the sudden pressure difference in this field. During the period examined in the figure, the temperatures around the projectile increased as it moved. In this case, the range of the highest temperature values occurring around the projectile was 400-420 K at 0.46 ms, 540-560 K at 0.56 ms and 560-580 K at 0.68 ms.

The variation graphs of pressure, velocity and temperature with time at different points (x:120 mm, y:5 mm, 25 mm, 45 mm) for subsonic and supersonic projectiles was shown in Fig. 8. In this context, only the results of RNG k-ε turbulence model for subsonic projectile and Spalart-Allmaras turbulence model

for supersonic projectile were given in which the SPL_{peak} values were best estimated in comparison to experiments. When the graphs were examined, the peak temperature and velocity values for subsonic and supersonic projectiles decreased as the y-distance increased. On the other hand, the highest peak pressure occurred at x:120 and y:25 in both projectile models. The subsonic projectile reached the computational domain boundary in about 2.5 milliseconds, while this time was approximately 2 ms for the supersonic projectile. Similarly, the peak pressure, temperature and velocity values occurred approximately at 0.5 ms for subsonic projectile, while the peak values occurred approximately at 0.4 ms for supersonic projectile. Peak velocities occur at the moment of instantaneous pressure and temperature drops in both projectile types. Since the peak pressure, velocity and temperature values occurred at different times and locations in both projectile types, it was difficult to compare them at the same points. However, to give an idea, the two projectile models were compared for the same points. In this context, the peak pressures at all points were higher for supersonic projectile. The highest peak pressure was 1.88 atm for subsonic projectile, while it was 2.13 atm for supersonic projectile. The peak velocity value at the point of x:120 mm and y:5 mm was very close to each other and was approximately 1004 m/s in both projectile types. When the

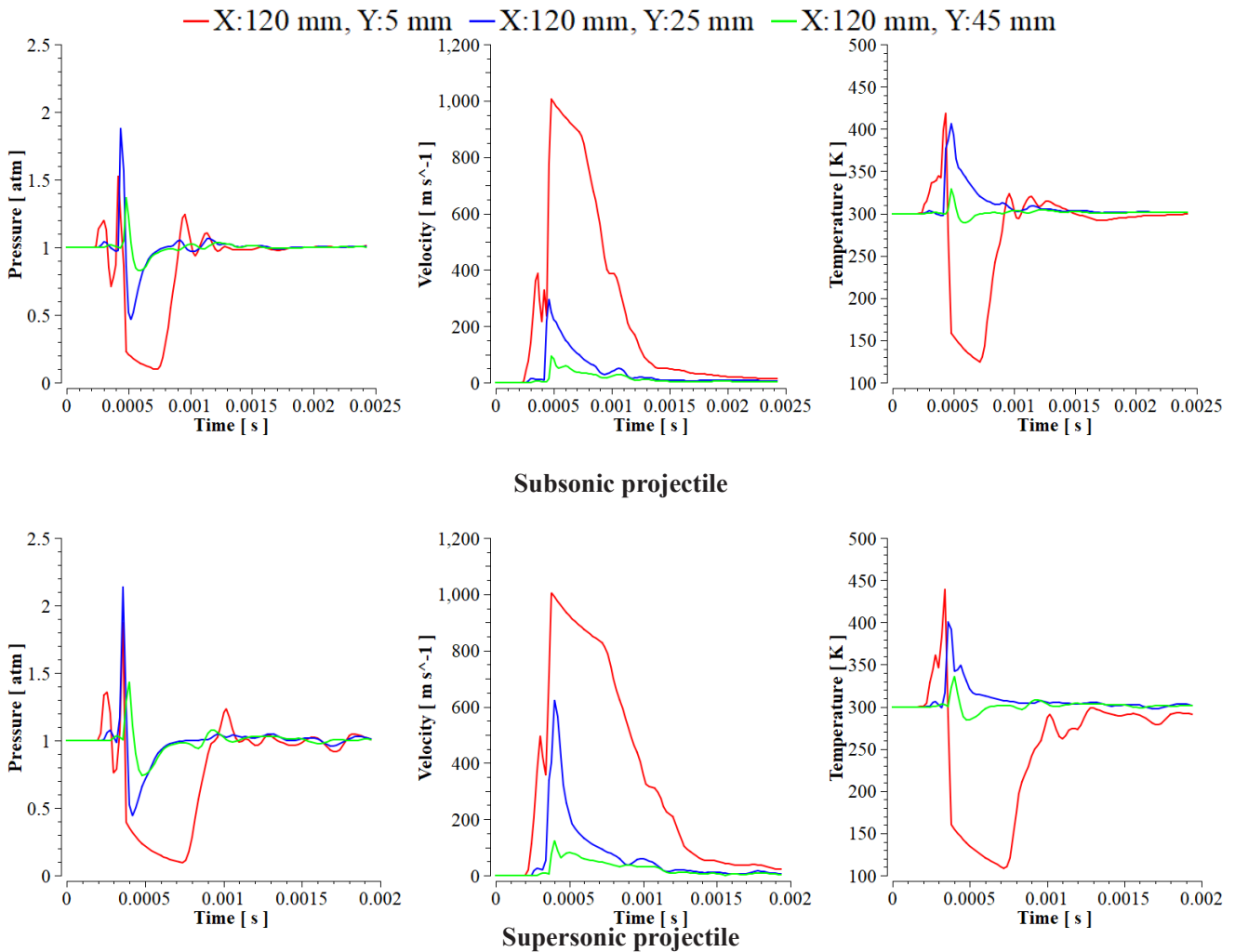


Figure 8. The variation graphs with time at different points.

temperature graph was examined, the peak temperature value at the point of $x:120$ mm and $y:5$ mm was higher for supersonic projectile, while it was very close to each other at other points. The highest peak temperature was 419.45 K for subsonic projectile, while it was 440.09 K for supersonic projectile. Pressures at the projectile base at the mouth of the barrel vary depending on many different parameters such as barrel length, barrel diameter, calculation domain, initial pressure and temperature. To give an idea, the approximate pressure values at the mouth of the barrel according to available literature were given in Table 3. In the given studies, it was seen that pressure value at the mouth of the barrel generally varied between 1.94 MPa and 25 MPa. In this study, the change of pressure at the projectile base depending on time was shown in Fig. 9. The projectile moved in the barrel for approximately 300 microseconds. While the pressure at the projectile base was initially 283.7 MPa, it gradually decreased over time and dropped to roughly 10 MPa at the mouth of the barrel.

Table 3. Approximate pressure values at the mouth of the barrel according to available literature

Literature	Calibre	Dimension	Pressure at the mouth of the barrel (MPa)
²⁹	9 mm	2 D	1.94
³⁰	9 mm	2 D	16.8
³¹	9 mm	2 D	-
³²	9 mm	3 D	25
³³	7.62 mm	3 D	16
Present study	9 mm	2 D	10

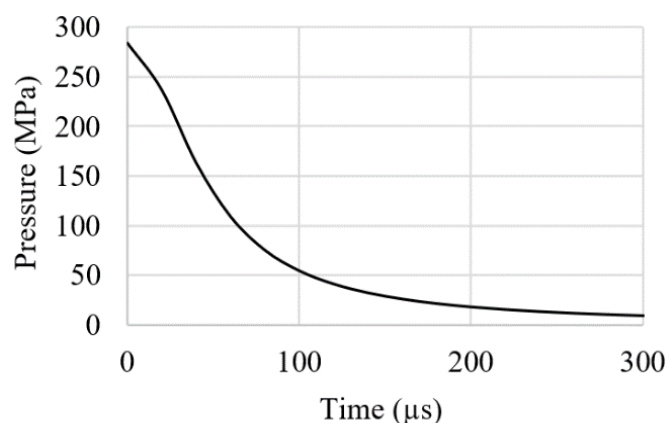


Figure 9. Change of pressure at the projectile base depending on time.

4. CONCLUSION

The purpose of this study was to estimate, using various turbulence models, the flow phenomena that take place in the near-field upon firing a 9x19 mm gun and the sound emitted in the far-field. In this context, experimental gunshot tests were conducted using subsonic and supersonic projectiles. The projectile velocities at the barrel exit and the SPL_{peak} values at different locations were measured experimentally, and the numerical model was validated according to these parameters. The Fluent package program was used to model flow and acoustic analysis together. The far-field noise was

calculated using the FW-H acoustics model. Analyzes were conducted under two-dimensional, axisymmetric and transient conditions. As turbulence models, k-ε models (Standard, RNG, Realizable), Standard k-ω, Spalart-Allmaras and LES turbulence models were used. The dynamic mesh was used to model the projectile motion.

4.1 Results Evaluation

In the experimental study, projectile velocities at the barrel exit were measured as 317 m/s for subsonic projectile and 382 m/s for the supersonic projectile. In the numerical model, the subsonic and supersonic projectile velocities at the barrel exit were calculated as 301 m/s and 375 m/s, respectively.

The best SPL_{peak} results were obtained with RNG k-ε turbulence model for subsonic projectile and Spalart-Allmaras turbulence model for supersonic projectile in comparison to experimental results.

For the subsonic projectile, the SPL_{peak} values at 1 m, 10 m and 30 m distances were experimentally measured as 164.8 dB, 143.1 dB, 132.6 dB, and were numerically estimated with RNG k-ε turbulence model as 164.8 dB, 142.9 dB, 133.2 dB, respectively. On the other hand, the peak sound pressures for the supersonic projectile at 1 m, 10 m and 30 m distances were experimentally measured as 166.8 dB, 152.9 dB, 143.3 dB and numerically estimated with Spalart-Allmaras turbulence model as 166.8 dB, 150.6 dB, 141.0 dB, respectively.

When the SPL_{peak} values were evaluated with turbulence models where the best results are obtained, the highest difference was 0.52 % at the distance of 5 m in the RNG k-ε turbulence model. On the other hand, the highest difference was 2.12 % at the distance of 2.5 m in the Spalart-Allmaras turbulence model.

SPL_{peak} values in Standard k-ε and RNG k-ε turbulence models occurred at lower frequencies compared to other turbulence models.

While the velocity and pressure values around the projectile decreased with time, the temperature increased during the period in which the contours were evaluated.

Among the turbulence models examined, the RNG turbulence model with an average absolute error of 0.234 % at subsonic speeds and the Spalart turbulence model with an average absolute error of 0.974 % at supersonic velocities were the most suitable turbulence models to use in estimating the far-field noise emitted from a small-caliber gun.

This study is valuable in providing researchers and manufacturers with ideas when producing firearms. Additionally, this study introduced an innovative method to the literature on combining flow and acoustic analyses in firearms. In future studies, it would be beneficial to investigate the effect of the three-dimensional computation domains, turbulence models in three-dimensional domain, positions and sizes of the sound sources on computational domain.

REFERENCES

1. Pater, L. & Shea, J. Techniques for reducing gun blast noise levels: An experimental study 1981, **61**.
2. Zhao, X.Y.; Zhou, K.D.; He, L.; Lu, Y.; Wang, J. & Zheng, Q. Numerical simulation and experiment on impulse noise in a small caliber rifle with muzzle brake. *Shock Vib.*, 2019, 5938034.

- doi: 10.1155/2019/5938034.
3. Lo, S.W.; Tai, C.H. & Teng, J.T. Axial-Symmetry numerical approaches for noise predicting and attenuating of rifle shooting with suppressors. *J. Appl. Math.*, 2011, 961457.
doi: 10.1155/2011/961457.
 4. Deng, Y.; Feng, J.; Wan, F.; Shen, X. & Xu, B. Evaluation of the turbulence model influence on the numerical simulation of cavitating flow with emphasis on temperature effect, *Processes*, 2020, **8**, 997.
doi: 10.3390/pr8080997.
 5. Joshi, J.B.; Nandakumar, K.; Patwardhan, A.W.; Nayak, A.K.; Pareek, V.; Gumulya, M.; Wu, C.; Minocha, N.; Pal, E.; Kumar, M.; Bhusare, V.; Tiwari, S.; Lote, D.; Mali, C.; Kulkarni, A. & Tamhankar, S. 2-Computational fluid dynamics. In: Joshi, J.B. and Nayak, A.K.B.T.-A. of C.F.D. in N.R.D. and S.A. (eds.) Woodhead Publishing Series in Energy. pp. 21–238. Woodhead Publishing, 2019.
 6. Christopher, N.; Peter, J.M.F.; Kloker, M.J. & Hickey, J.P. DNS of turbulent flat-plate flow with transpiration cooling. *Int. J. Heat Mass Transf.*, 2020, **157**, 119972.
doi: 10.1016/j.ijheatmasstransfer.2020.119972.
 7. Kumar, P. & Mahesh, K. Large-eddy simulation of flow over an axisymmetric body of revolution. *J. Fluid Mech.* 2018, **853**, 537–563.
doi: 10.1017/jfm.2018.585.
 8. Miltner, M.; Jordan, C. & Harasek, M. CFD simulation of straight and slightly swirling turbulent free jets using different RANS-turbulence models. *Appl. Therm. Eng.* 2015, **89**, 1117–1126.
doi: 10.1016/j.applthermaleng.2015.05.048.
 9. Hart, J. Comparison of turbulence modeling approaches to the simulation of a dimpled sphere. *Procedia. Eng.* 2016, **147**, 68–73.
doi: 10.1016/j.proeng.2016.06.191.
 10. Jiang, Z. Wave dynamic processes induced by a supersonic projectile discharging from a shock tube. *Phys. Fluids.*, 2003, **15**, 1665–1675.
doi: 10.1063/1.1566752.
 11. Luo, Y.; Xu, D. & Li, H. Analysis of the dynamic characteristics of the muzzle flow field and investigation of the influence of projectile nose shape. *Appl. Sci.*, 2020, **10**(4), 1468.
doi: 10.3390/app10041468.
 12. Czyżewska, M. & Trębiński, R. Wpływ urządzenia wylotowego lufy na przyrost prędkości pocisku w okresie balistyki przejściowej. *Probl. Mechatronics. Armament, Aviat. Saf. Eng.*, 2015, **6**, 87–98.
doi: 10.5604/20815891.1157779.
 13. Kikuchi, Y.; Ohnishi, N. & Ohtani, K. Experimental demonstration of bow-shock instability and its numerical analysis. *Shock Waves.*, 2017, **27**, 423–430.
doi: 10.1007/s00193-016-0669-5
 14. Kang, K.J.; Ko, S.H. & Lee, D.S. A study on impulsive sound attenuation for a high-pressure blast flowfield. *J. Mech. Sci. Technol.*, 2008, **22**, 190–200.
doi: 10.1007/s12206-007-1023-8
 15. Xavier, S. Numerical analysis of gun barrel pressure blast using dynamic mesh adaption, Embry-Riddle Aeronautical University Dissertations and Theses, 2011.
 16. Huerta-Torres, J.; Silva-Rivera, U.; Verduzco-Cedeño, V.; Flores-Herrera, L. & Sandoval-Pineda, J. Numerical and experimental analysis of sound suppressor for a 5.56 mm Calibre. *Def. Sci. J.*, 2021, **71**.
doi: 10.14429/dsj.71.14957.
 17. Hudson, M.; Luchini, C.; Clutter, K. & Shyy, W. CFD approach to firearms sound suppressor design. In 32nd Joint Propulsion Conference and Exhibit, 1996.
doi: 10.2514/6.1996-3020
 18. Bin, J.; Kim, M. & Lee, S. A numerical study on the generation of impulsive noise by complex flows discharging from a muzzle. *Int. J. Numer. Methods Eng.*, 2008, **75**, 964–991.
doi: 10.1002/nme.2291.
 19. Lee, I.C.; Lee, D.J.; Ko, S.H.; Lee, D.S. & Kang, G.J. Numerical analysis of a blast wave using CFD-CAA Hybrid Method. In 12th AIAA/CEAS Aeroacoustics Conf. 27th AIAA Aeroacoustics Conf., American Institute of Aeronautics and Astronautics; 2006.
doi: 10.2514/6.2006-2701.
 20. Wang, Y.; Jiang, X.H.; Yang, X.P. & Guo, Z.Q. Numerical simulation on jet noise induced by complex flows discharging from small caliber muzzle. *Baozha Yu Chongji/Explosion Shock Waves*, 2014, **34**, 508–512.
doi: 10.11883/1001-1455(2014)04-0508-05.
 21. Zhao, X. & Lu, Y. A comprehensive performance evaluation method targeting efficiency and noise for muzzle brakes based on numerical simulation. *Energies*, 2022, **15**.
doi: 10.3390/en15103576.
 22. Gurdamar, O.; Ozbektas, S. & Sungur, B. Analysis of the effect of circular ring baffles in suppressor on flow field and far field noise levels at 9 mm semi-automatic pistol. *Def. Sci. J.*, 2023, **75**(5), 531-540.
 23. Gurdamar, O.; Ozbektas, S. & Sungur, B. Experimental investigation of the projectile type on sound pressure levels fired with 9 mm gun. *Khazar J. Sci. Technol.*, 2022, **6**(1), 96–104.
doi: 10.5782/2520-6133.2022.6.1.96
 24. Ansys user guide. Fluent, Ver. 18, Ansys Fluent Tutorial Guide. Ansys Inc., Canonsburg, PA, 2017.
 25. Kaltenbacher, M.; Escobar, M.; Becker, S. & Ali, I. Computational aeroacoustics based on lighthill's acoustic analogy. In: Marburg, S., Nolte, B. (eds) Computational Acoustics of Noise Propagation in Fluids - Finite and Boundary Element Methods. pp. 115-142. Springer, 2008.
doi:10.1007/978-3-540-77448-8_5.
 26. Li, Y.M.; Li, B.K.; Qi, F.S. & Wang, X.C. Numerical investigation of the interaction of the turbulent dual-jet and acoustic propagation. *Chinese Phys. B.*, 2017, **26**, 24701.
doi: 10.1088/1674-1056/26/2/024701.
 27. Qin, Q. & Zhang, X. Numerical investigation on combustion in muzzle flows using an inert gas labeling method. *Int. J. Heat Mass Tran.*, 2016, **101**, 91-

103.
doi: 10.1016/j.ijheatmasstransfer.2016.05.009.
28. Hellberg, V. & Fredriksson, R. Calculation of fluid dynamic loads on a projectile during firing: Development of a CFD-modelling Approach. 2016.
29. Tavana, M.S.P.; Alavi, S.A.H.; Rahmati, S. & Fazeli, H. Interior Ballistic Simulation for 9 mm Gun for bullet and blank shot applying spalart-allmars turbulence model. *Rom. J. Acoust. Vib.*, 2022, **19**(2), 75-85.
30. Bougamra, A. & Lu, H.L. Multiphase CFD simulation of solid propellant combustion in a small gun chamber. *Int. J. Chem. Eng.*, 2014, **2014**, 1-10.
doi: 10.1155/2014/971808.
31. Silva-Rivera, U.S.; Zúñiga-Avilés, L.A.; Vilchis-González, A.H.; Tamayo-Meza, P.A. & Wong-Angel, W.D. Internal ballistics of polygonal and grooved barrels: A comparative study. *Sci. Prog.*, 2021, **104**(2), 368504211016954.
doi: 10.1177/00368504211016954.
32. Deng, S.; Sun, H.K.; Chiu, C.J. & Chen, K.C. Transient finite element for in-bore analysis of 9 mm pistols. *Appl. Math. Model.*, 2014, **38**(9-10), 2673-2688.
doi: 10.1016/j.apm.2013.10.071.
33. Rivera, U.S.S.; Pinede, J.M.S.; Susarrey-Huerta, O.; Herrera, L.A.F. & Mezag, P.A.T. Numerical modelling of caseless ammunition with coreless bullet in internal

ballistics. *Defence Sci. J.*, 2015, **65**(3), 203-207.
doi: 10.14429/dsj.65.8511

CONTRIBUTORS

Mr Seyda Ozbektas obtained his MSc degree and working as a Research Assistant at the Mechanical Engineering Department of Ondokuz Mayıs University in Samsun, Turkey. His areas of research include: Firearms and numerical investigations of internal and terminal ballistics problems.

His contribution to the current study: Software, validation, formal analysis, investigation, visualisation.

Dr Bilal Sungur obtained his PhD in Mechanical Engineering from the Ondokuz Mayıs University, Samsun, Turkey. He is currently working as an Assistant Professor at the Mechanical Engineering Department of Samsun University, Samsun, Turkey. His research interests include: Numerical modelling and analysis of firearms.

His contribution to the current study: Conceptualisation, software, writing, original draft preparation, supervision.

Mr Onur Gurdamar obtained his MSc degree and working at the Samsun Yurt Savunma company as R&D engineer. His areas of research include: Experimental investigations of firearms. His contribution to the current study: Validation, investigation, data curation.